

Excitation of Low-Frequency QPOs in Black Hole Accretion Flows

Mami MACHIDA

*Division of Theoretical Astronomy, National Astronomical Observatory of Japan,
2-21-1 Osawa, Mitaka-shi, Tokyo 181-8588*

mami@th.nao.ac.jp

and

Ryoji MATSUMOTO

*Department of Physics, Faculty of Science, Chiba University,
1-33 Yayoi-cho, Inage-ku, Chiba 263-8522*

matumoto@astro.s.chiba-u.ac.jp

(Received 2000 December 31; accepted 2001 January 1)

Abstract

We present the results of global three dimensional magneto-hydrodynamic simulations of black hole accretion flows. We focus on the dependence of numerical results on the gas temperature T_{out} supplied from the outer region. General relativistic effects are taken into account using the pseudo-Newtonian potential. We ignore the radiative cooling of the accreting gas. The initial state is a torus whose density maximum is at $35r_s$ or $50r_s$ from the gravitating center, where r_s is the Schwarzschild radius. The torus is initially threaded by a weak azimuthal magnetic field. We found that mass accretion rate and the mass outflow rate strongly depend on the temperature of the initial torus. The ratio of the average Maxwell stress generated by the magneto-rotational instability (MRI) to gas pressure, $\alpha \equiv \langle B_\varpi B_\varphi / 4\pi \rangle / \langle P \rangle$ is $\alpha \sim 0.05$ in the hot torus ($T_{\text{out}} \sim 9.5 \times 10^9 \text{K}$ at $50r_s$) and $\alpha \sim 0.01$ in the cool torus ($T_{\text{out}} \sim 1.1 \times 10^9 \text{K}$ at $35r_s$). In the cool model, a constant angular momentum inner torus is formed around $4 - 8r_s$. This inner torus deforms itself from a circle to a crescent quasi-periodically. During this deformation, the mass accretion rate, the magnetic energy and the Maxwell stress increase. As the magnetic energy is released, the inner torus returns to a circular shape and starts the next cycle.

Power spectral density (PSD) of the time variation of the mass accretion rate in the cool model has a low frequency peak around 10Hz when we assumed a $10M_\odot$ black hole. The PSD of the hot model is flat in 1 – 30Hz. The slope of the PSD in the cool model is steeper than that in the hot model in 30 – 100Hz. The mass outflow rate in the low temperature model also shows quasi-periodic oscillation. Intermittent

outflows are created in both models. The outflow speed is $0.01c - 0.05c$. The mass outflow rate is comparable to the mass accretion rate \dot{M} at $2.5r_s$ in the high temperature model and about $0.02\dot{M}$ in the low temperature model.

Key words: accretion, accretion disks—black hole physics—magnetohydrodynamics:MHD—QPO—dynamo

1. Introduction

Accretion disks are believed to be the energy source of various activities in active galactic nuclei, X-ray binaries, protostars and so on. Using the RXTE satellite, detailed timing analysis of X-ray binaries has been carried out (e.g., Homan et al. 2005, McClintock & Remillard 2006, Shaposhnikov et al. 2006). Black hole candidates (BHCs) show transitions between a low/hard state (LHS) dominated by the hard power-law component and a high/soft state (HSS) characterized by the soft black body component. During the transition, BHCs stay in hard intermediate state (HIMS) or in a soft intermediate state (SIMS) (Homan & Belloni 2005). The light curves during LHS of BHCs are subject to violent X-ray fluctuations and sometimes accompany quasi-periodic oscillations (QPO) in the Fourier Power Spectral Density (PSD). The LHS is associated with steady outflows (e.g., Gallo et al. 2003). In this state, mass accretes to the black hole as an optically thin, advection-dominated accretion flow (e.g., Ichimaru 1977; Narayan & Yi 1994, 1995). The energy spectrum of the HIMS is softer than that in the LHS. Low frequency ($1 - 10\text{Hz}$) QPOs are observed in the luminous hard state and in the intermediate state (McClintock & Remillard 2006). High frequency QPOs ($\sim 100\text{Hz}$) are sometimes observed in these states. The frequency of low-frequency QPOs in the intermediate state moves to higher frequency and the low-frequency QPOs disappear when the state changes to HSS (see Belloni et al. 2006).

These observations indicate that QPOs are associated with the cooling of the disk. By carrying out global three-dimensional (3D) magneto-hydrodynamic (MHD) simulations including radiative cooling, Machida et al. (2006) showed that when the accretion rate exceeds the limit for the onset of the cooling instability, the radiatively inefficient, optically thin disk transitions into a magnetically supported, cool, intermediate state. Oda et al. (2007) constructed a steady model of such disks and showed that their luminosity can exceed $0.1L_{\text{Edd}}$, where L_{Edd} is the Eddington luminosity. When the transition to the cool disk takes place in the outer region, cool gas will be supplied to the inner region.

Low frequency QPOs are sometimes attributed to the oscillation at the interface between the hot inner disk and the cool outer disk (e.g., Di Matteo & Psaltis 1999). The excitation mechanism of such an oscillation, however, was not clear. Another puzzle is the coexistence of low-frequency and high-frequency QPOs. Abramowicz & Kułźniak (2001) proposed that

high-frequency QPOs are generated by the resonance between radial and vertical oscillations of accretion disks. S. Kato (2001a,b) pointed out that non-axisymmetric g-mode oscillations can be trapped in a thin, relativistic disk and these oscillations are excited by the corotation resonance. Non-linear couplings of disk oscillations and disk warp were examined by S. Kato (2004).

Y. Kato (2004b) reproduced high-frequency QPOs by 3D MHD simulations of optically thin, geometrically thick accretion flows. They showed that the QPOs appear around the epicyclic frequency κ at $4r_s$ and $\Omega + \kappa$, where Ω is the Kepler frequency and showed that the amplitude of QPOs are damped after a while.

The $1/f$ -noise-like fluctuations observed in BHCs have been reproduced by global 3D MHD simulations (e.g., Kawaguchi et al. 2000, Hawley 2001). Kawaguchi et al. (2000) showed that the PSD changes its slope around 10 Hz when they assumed a $10M_\odot$ black hole. Machida & Matsumoto (2003) pointed out that magnetic reconnection in the innermost region of the disk can be the origin of intermittent X-ray flares known as X-ray shots (Negoro et al. 1995), which produce flat PSD at low-frequency (~ 1 Hz).

In this paper, we report the results of global 3D MHD simulations which produced low-frequency QPOs and discuss their excitation mechanisms.

In section 2, we describe basic equations and initial conditions. The results of simulations are given in section 3. In section 4, we concentrate on the oscillation excited in the inner torus. Section 5 is devoted to discussion and conclusion.

2. Numerical Methods

2.1. Basic Equations

We solved the following resistive MHD equations in a cylindrical coordinate system (ϖ, φ, z) ;

$$\frac{\partial \rho}{\partial t} + \nabla \cdot (\rho \mathbf{v}) = 0 , \quad (1)$$

$$\rho \left[\frac{\partial \mathbf{v}}{\partial t} + \mathbf{v} \cdot \nabla \mathbf{v} \right] = -\nabla P - \rho \nabla \phi + \frac{\mathbf{j} \times \mathbf{B}}{c} , \quad (2)$$

$$\frac{\partial \mathbf{B}}{\partial t} = \nabla \times (\mathbf{v} \times \mathbf{B} - \frac{4\pi}{c} \eta \mathbf{j}) , \quad (3)$$

$$\rho T \frac{dS}{dt} = \frac{4\pi}{c^2} \eta j^2 , \quad (4)$$

where ρ , P , ϕ , \mathbf{v} , \mathbf{B} , $\mathbf{j} = c \nabla \times \mathbf{B} / 4\pi$, η , T , and S are the density, pressure, gravitational potential, velocity, magnetic field, current density, resistivity, temperature and specific entropy, respectively. The specific entropy is expressed as $S = C_v \ln(P/\rho^\gamma)$, where C_v is the specific heat capacity and γ is the specific heat ratio. We included the Joule heating term but neglected the radiative cooling term in the energy equation. We assume the anomalous resistivity $\eta = \eta_0 [\max(v_d/v_c - 1, 0)]^2$ (Yokoyama & Shibata 1994), where $v_d \equiv j/\rho$ is the electron-ion drift speed and v_c is the threshold above which anomalous resistivity sets in.

General relativistic effects are simulated using the pseudo-Newtonian potential $\phi = -GM/(r - r_s)$ (Paczynski & Witta 1980), where G is the gravitational constant, M is the mass of the black hole, $r = (\varpi^2 + z^2)^{1/2}$, and r_s is the Schwarzschild radius. We neglect the self-gravity of the disk.

2.2. Numerical Methods and Boundary Conditions

We solved the resistive MHD equations using a modified Lax–Wendroff scheme (Rubin & Burstein 1967) with an artificial viscosity (Richtmyer & Morton 1967).

The units of length and velocity are the Schwarzschild radius r_s and the light speed c , respectively. The unit time is $t_0 = r_s c^{-1} = 10^{-4} M / 10 M_\odot$ s. The unit temperature is given by $T_0 = m_p c^2 k_B^{-1} = 1.1 \times 10^{13}$ K, where m_p is the proton mass and k_B is the Boltzmann constant.

The number of grids is $(N_\varpi, N_\varphi, N_z) = (250, 64, 384)$. The grid size is $\Delta\varpi = \Delta z = 0.1$ for $0 < \varpi/r_s < 10$, and $|z|/r_s < 10$. For model LT, we set the grid interval as follows; $\Delta\varpi_n = \min(1.05\Delta\varpi_{n-1}, \Delta\varpi_{\max})$, $\Delta z_n = \min(1.05\Delta z_{n-1}, \Delta z_{\max})$, where $\Delta\varpi_{\max} = 10\Delta\varpi$ and $\Delta z_{\max} = 10\Delta z$. The outer boundaries at $\varpi = 132r_s$ and at $z = \pm 70r_s$ are free boundaries where waves can be transmitted. For model HT, we set $\Delta\varpi_{\max} = 20\Delta\varpi$ and $\Delta z_{\max} = 100\Delta z$. Therefore, the outer boundaries are located at $\varpi = 230r_s$ and $z = \pm 170r_s$, respectively. The grid size in the azimuthal direction is $\Delta\varphi = 2\pi/63$.

We included the full circle ($0 \leq \varphi \leq 2\pi$) in the simulation region, and applied periodic

boundary conditions in the azimuthal direction. An absorbing boundary condition is imposed at $r = r_{\text{in}} = 2r_s$ by introducing a damping factor,

$$D = 0.1 \left(1.0 - \tanh \frac{r - r_{\text{in}} + 5\Delta\varpi}{2\Delta\varpi} \right). \quad (5)$$

The physical quantities $q = (\rho, \mathbf{v}, \mathbf{B}, P)$ inside $r = r_{\text{in}}$ are re-evaluated by

$$q^{\text{new}} = q - D(q - q_0), \quad (6)$$

which means that the deviation from initial values q_0 is artificially reduced with damping rate D . Waves propagating inside $r = r_{\text{in}}$ are absorbed in the transition region $(r_{\text{in}} - 5\Delta\varpi < r < r_{\text{in}})$.

2.3. Initial Model

The initial state of our simulation is an equilibrium torus threaded by a weak toroidal magnetic field. At the initial state, the torus is assumed to have a specific angular momentum, $L \propto \varpi^a$.

The magnetic field distribution is determined according to Okada et al. (1989). By using the polytropic relation $P = K\rho^\gamma$ at the initial state and by assuming

$$\beta = \frac{8\pi P}{B_\varphi^2} = \beta_b \left(\frac{\varpi}{\varpi_b} \right)^{-2(\gamma-1)}, \quad (7)$$

where β_b is the initial plasma β at the initial pressure maximum of the torus $(\varpi, z) = (\varpi_b, 0)$, and B_φ is the azimuthal magnetic field. We integrated the equation of motion into a potential form,

$$\Psi(\varpi, z) = \phi + \frac{L^2}{2\varpi^2} + \frac{1}{\gamma-1} v_s^2 + \frac{\gamma}{2(\gamma-1)} v_A^2 = \Psi_b = \text{constant}, \quad (8)$$

where $v_s = (\gamma P/\rho)^{1/2}$ is the sound speed, $v_A = B_\varphi/(4\pi\rho)^{1/2}$ is the Alfvén speed, and $\Psi_b = \Psi(\varpi_b, 0)$. At $\varpi = \varpi_b$, the rotation speed of the torus L/ϖ_b equals the Keplerian velocity. By using equation (8), we obtain the density distribution as

$$\rho = \rho_b \left\{ \frac{\max[\Psi_b - \phi - L^2/(2\varpi^2), 0]}{K[\gamma/(\gamma-1)][1 + \beta_b^{-1}\varpi^{2(\gamma-1)}/\varpi_b^{2(\gamma-1)}]} \right\}^{1/(\gamma-1)}, \quad (9)$$

where ρ_b is the density at $(\varpi, z) = (\varpi_b, 0)$. Outside the torus, we assumed a hot, isothermal ($T = T_{\text{halo}}$) spherical halo. The density distribution of the halo is given by $\rho_h = \rho_{\text{halo}} \exp[-(\phi - \phi_b)/(k_B T_{\text{halo}})]$, where ϕ_b is the gravitational potential at $(\varpi, z) = (\varpi_b, 0)$.

In this paper, we report the results of simulations for two models. Model HT assumes a hot outer torus with the sound speed $c_b = 0.029c$ at $\varpi_b = 50r_s$. In model HT, the torus has a constant specific angular momentum ($a = 0$). Model LT is a cool disk model in which $c_b = 0.01c$ at $\varpi_b = 35r_s$ and $a = 0.43$. In both models, we adopted $\beta_b = 100$, $\gamma = 5/3$, $L = (\varpi_b/2)^{1/2}\varpi_b/(\varpi_b - 1)\varpi^a$, $\rho_{\text{halo}} = 10^{-4}\rho_b$, $\eta_0 = 5 \times 10^{-4}$, and $v_c = 0.9c$. Since we do not include radiative cooling, ρ_b is arbitrary. We adopt $\rho_b = 1$.

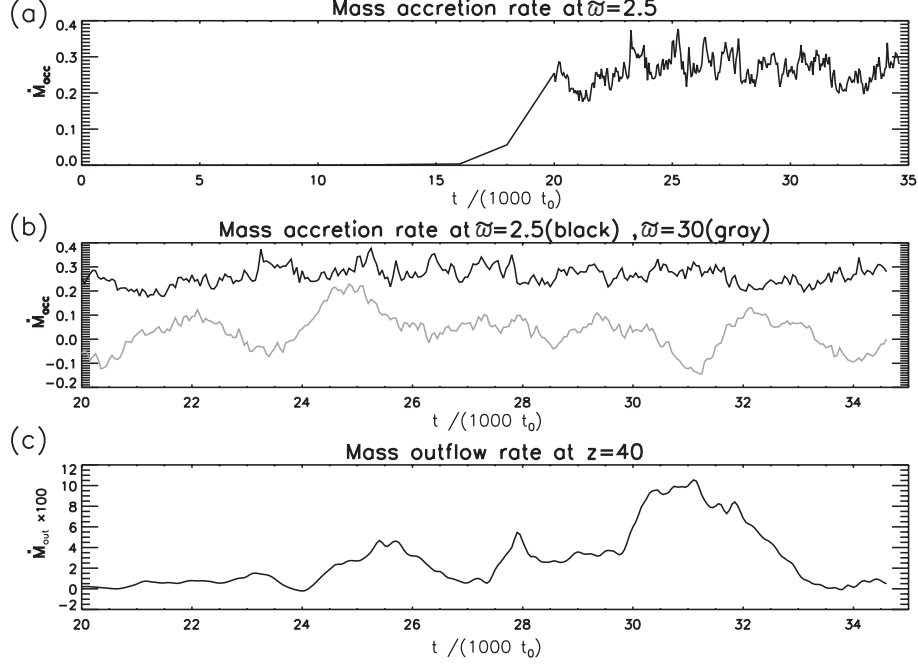


Fig. 1. (a) Time evolution of the mass accretion rate for model HT measured at $\varpi = 2.5r_s$. (b) Time evolution of the mass accretion rate at $\varpi = 2.5r_s$ (black) and $\varpi = 30r_s$ (gray). (c) Mass outflow rate measured at $z = 40r_s$.

3. Numerical Results

3.1. A hot accretion disk : model HT

Figure 1a shows the time evolution of mass accretion rate for model HT measured at $\varpi = 2.5r_s$. Figure 1b shows the time evolution of mass accretion rate at $\varpi = 2.5r_s$ (black) and at $\varpi = 30r_s$ (gray). The mass accretion rate \dot{M} at $\varpi = 2.5r_s$ is computed by

$$\dot{M} = \int_{-20}^{20} \int_0^{2\pi} \rho \varpi v_{\varpi} d\varphi dz . \quad (10)$$

The mass accretion rate at $\varpi = 30r_s$ is measured by integrating the accretion rate in the equatorial region $|z| < 5r_s$. The unit of the mass accretion rate is $\dot{M}_0 = 2\pi\rho_b r_s^2 c$. Mass accretion rate at $\varpi = 2.5r_s$ becomes quasi-steady after about 10 rotational periods at the initial density maximum. The increase in mass accretion rate saturates when $\dot{M} \sim 0.3\dot{M}_0$. The mass accretion takes place due to the efficient angular momentum transport by Maxwell stress in an MRI-driven turbulent field. The equatorial mass accretion rate at $\varpi = 30r_s$ shows time variation with a timescale of $\sim 4000t_0$. Figure 1c shows the time evolution of mass outflow rate measured at $z = 40r_s$ computed by

$$\dot{M}_{out} = \int_2^{43} \int_0^{2\pi} \rho v_z \varpi d\varphi d\varpi . \quad (11)$$

The mass outflow rate correlates with the mass accretion rate with a time lag of about $4000t_0$.

Figure 2a shows the correlation between the mass accretion rate at $\varpi = 2.5r_s$ and the

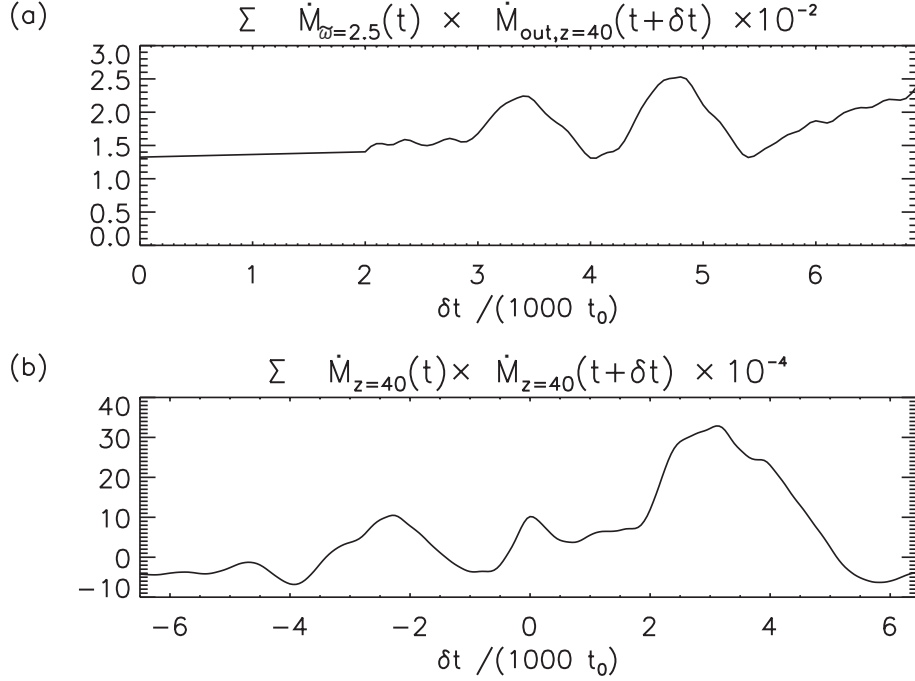


Fig. 2. (a) Correlation between the mass accretion rate at $\varpi = 2.5r_s$ and the mass outflow rate at $z = 40r_s$.
(b) Self correlation of the mass outflow rate at $z = 40r_s$.

mass outflow rate measured at $z = 40r_s$ for model HT. The correlation is computed by

$$F(\delta t) = \int_{t_s}^{t_e} [(A(t) - \bar{A}) \cdot (B(t + \delta t) - \bar{B})] dt. \quad (12)$$

Here, \bar{A} and \bar{B} are average during the interval $t_s < t < t_e$. In figure 2, we adopted $t_s = 18000t_0$ and $t_e = 25000t_0$. The correlation function has peaks at $\delta t = 3400t_0$ and $\delta t = 4800t_0$. The mass outflow rate at $z = 40r_s$ correlates with the mass accretion rate at $\varpi = 2.5r_s$ with delay of $3000t_0 - 5000t_0$. This timescale is comparable to the time scale of the propagation time of the outflow whose average speed is $\sim 0.01c$. Figure 2b shows the self correlation function of the mass outflow rate at $z = 40r_s$ in the time interval $21500 < t/t_0 < 33500$. In addition to the peak at $\delta t = 0$, positive peaks appear around $\delta t = -2400t_0$ and $\delta t = 2400t_0$. This indicates that mass outflow rate oscillates quasi-periodically with period $\sim 2400t_0$.

Figure 3 shows the isosurface of the density and the vertical velocity. Blue surfaces and green surfaces depict the density isosurface ($\rho = 0.2$) and the isosurface of vertical velocity ($v_z = 0.05c$), respectively. Winds emerge intermittently from the inner region of the accretion disk. Toroidal magnetic fields are dominant in the wind. The intermittent ejection is driven by expansion of magnetic loops anchored to the accretion disk (Y. Kato et al. 2004a).

Figure 4a shows the time evolution of magnetic energy integrated in $4 < \varpi/r_s < 10$, and $|z|/r_s < 1$ normalized by the initial gas pressure at $(\varpi, z) = (\varpi_b, 0)$. Figure 4b shows the time evolution of $B_{\varpi}^2/8\pi$ averaged in $4 < \varpi/r_s < 10$, and $|z|/r_s < 1$. Figures 4c and 4d

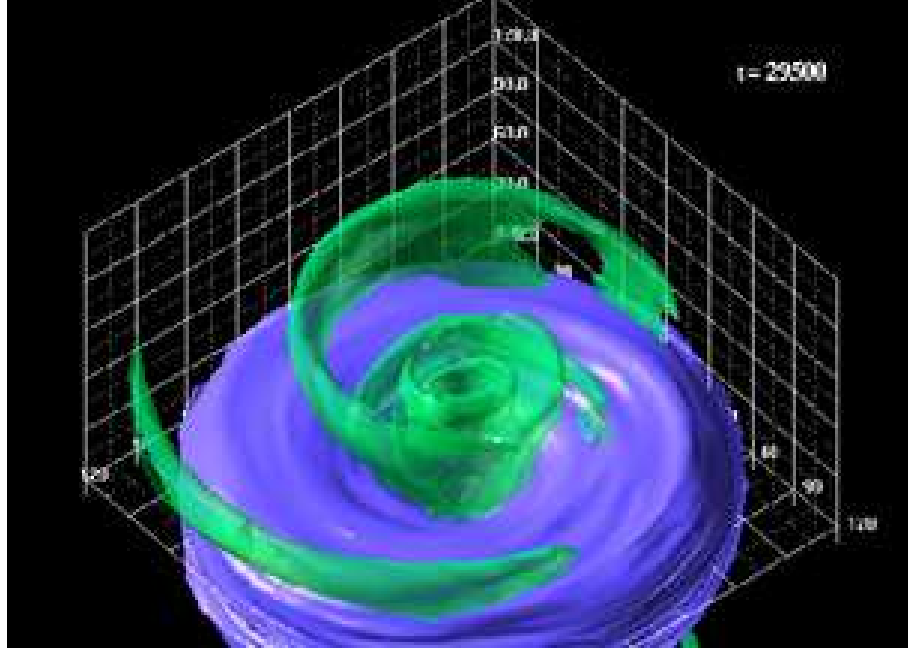


Fig. 3. Emergence of outflows from the inner region of the disk. Blue surfaces show the isosurface of the density ($\rho = 0.2$) for model HT at $t = 29500t_0$. Green surfaces show the isosurface of the vertical velocity ($v_z = 0.05c$).

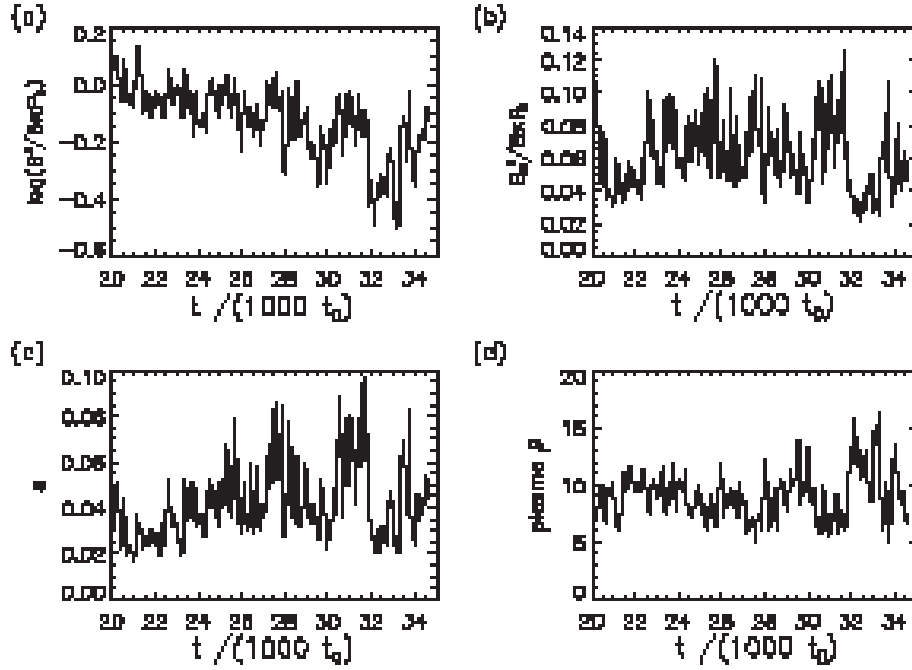


Fig. 4. Time evolution of physical quantities for model HT averaged in $4 < \varpi/r_s < 10$, $|z|/r_s < 1$, and $0 \leq \varphi \leq 2\pi$. (a) Magnetic energy, (b) $\langle B_\varpi^2/8\pi \rangle/P_b$, (c) time evolution of angular momentum transport rate, and (d) time evolution of the plasma β .

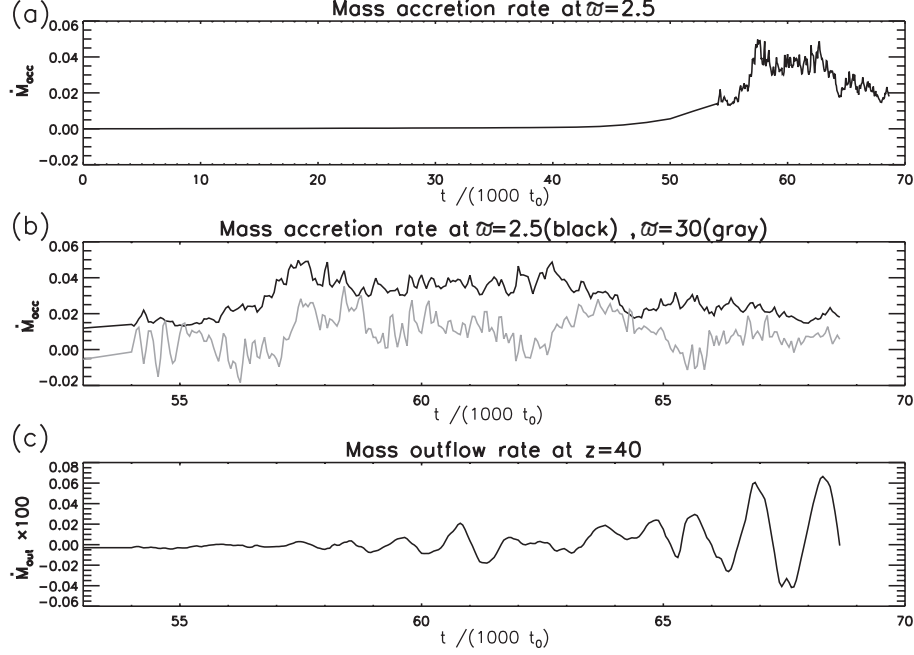


Fig. 5. (a) Time development of the mass accretion rate \dot{M} at $\varpi = 2.5r_s$ for model LT. (b) Time evolution of the mass accretion rate \dot{M} at $\varpi = 2.5r_s$ (black) and the equatorial mass accretion rate at $\varpi = 30r_s$ (gray). The interval $53000 < t/t_0 < 70000$ is enlarged. (c) Mass outflow rate at $z = 40r_s$ for model LT.

show the time evolution of $\alpha \equiv \langle B_\varpi B_\phi / 4\pi \rangle / \langle P \rangle$ and the ratio of the gas pressure to magnetic pressure $\beta \equiv P_{\text{gas}} / P_{\text{mag}}$, respectively. Although magnetic energy decreases, the plasma β is nearly constant ($\beta \sim 8$) because gas pressure also decreases. The fluctuations of the magnetic energy and radial magnetic field correlate with the mass accretion rate.

3.2. A cool accretion disk: model LT

Figure 5a shows the time evolution of the mass accretion rate for model LT measured at $\varpi = 2.5r_s$. Figure 5b shows the mass accretion rate at $\varpi = 2.5r_s$ (black) and the equatorial mass accretion rate at $\varpi = 30r_s$ (gray) which enlarges the time range $53000 < t/t_0 < 70000$. Figure 5c shows the time evolution of the mass outflow rate measured at $z = 40r_s$. In Figure 5a, $\dot{M} \sim 0.04\dot{M}_0$ is an order of magnitude smaller than that for model HT. This result indicates that the angular momentum transport rate strongly depends on the temperature of the gas supplied from the outer region.

Figure 6a shows the correlation between the mass accretion rate at $\varpi = 2.5r_s$ and the mass outflow rate at $z = 40r_s$ in the interval $52000 < t/t_0 < 62000$ for model LT. The mass outflow rate correlates with the mass accretion rate with time delay of $5000t_0 - 6000t_0$. Figure 6b shows the self correlation of the mass outflow rate at $z = 40r_s$ in the interval $56650 < t/t_0 < 68650$. Positive peaks appear at $\delta t/t_0 = -1500, 0, 2400, 3500$, and 4700 . It indicates that the mass outflow rate oscillates with period $1000t_0 - 2000t_0$.

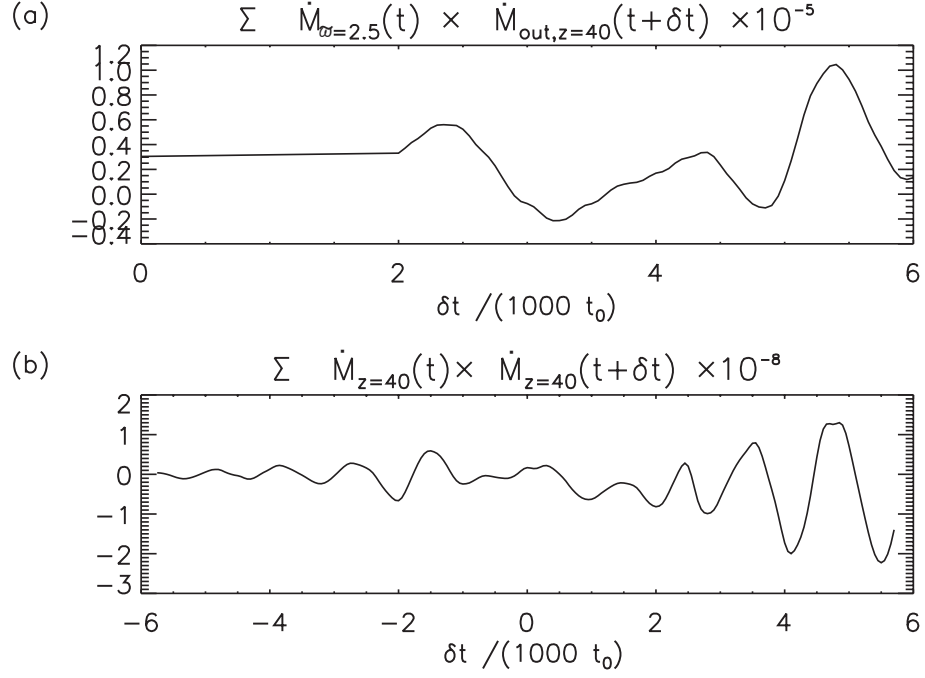


Fig. 6. (a) Correlation between the mass accretion rate at $\varpi = 2.5r_s$ and mass outflow rate at $z = 40r_s$. (b) Self correlation of the mass outflow rate at $z = 40r_s$.

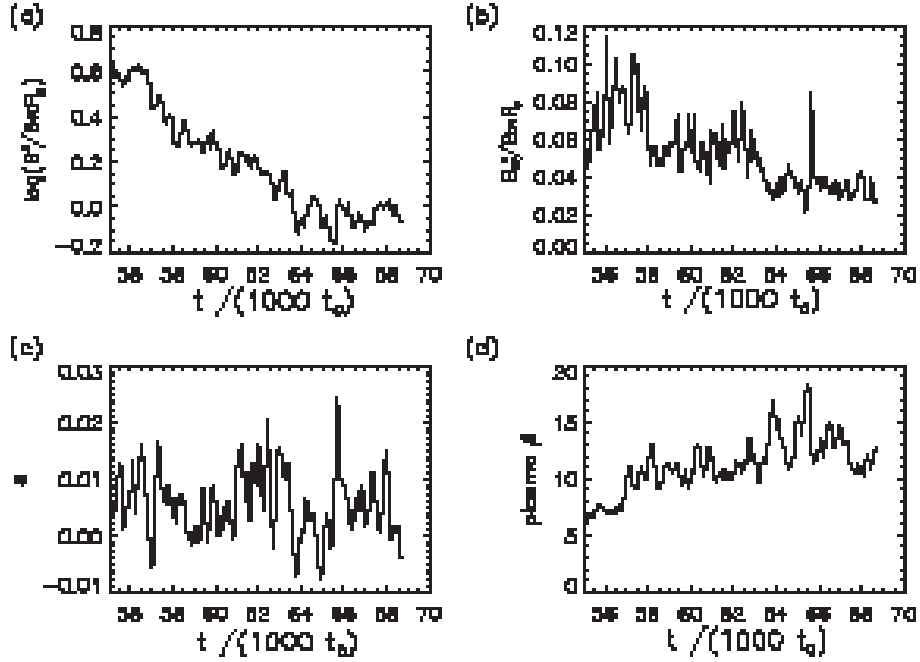


Fig. 7. Time evolution of (a) magnetic energy, (b) radial magnetic field, (c) angular momentum transport rate and (d) plasma β for model LT.

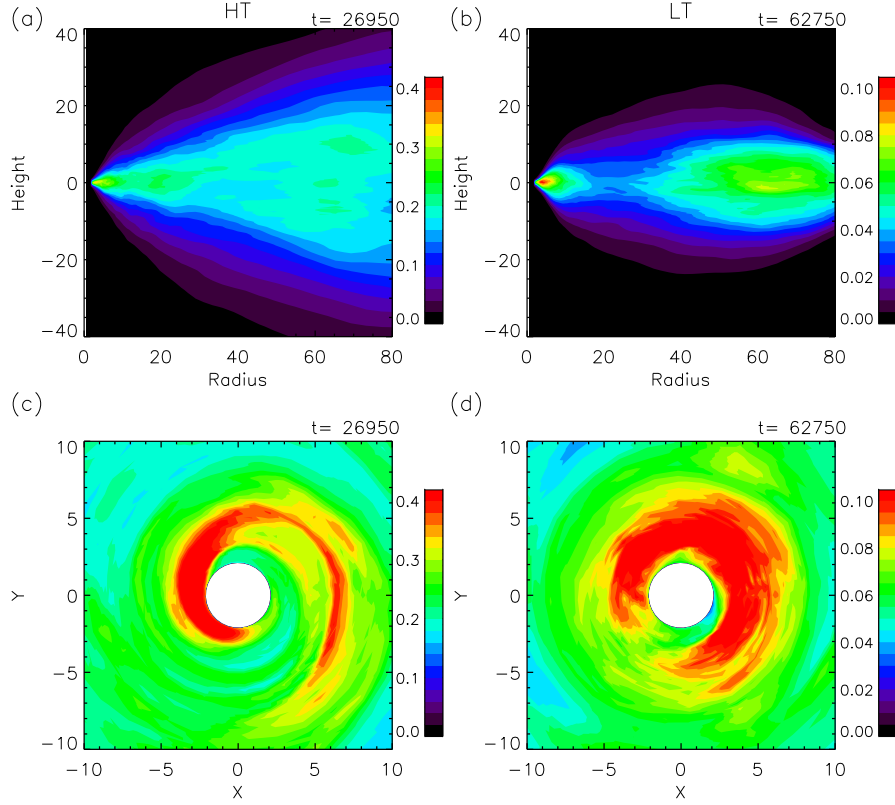


Fig. 8. The snapshots of the density distribution for model HT (left) and model LT (right). (a) and (b) show the density distribution averaged in the azimuthal direction. (c) and (d) show the density averaged in $|z|/r_s < 1$.

Figure 7 shows the time evolution of (a) magnetic energy, (b) $\langle B_{\varpi}^2/8\pi \rangle/P_b$, (c) angular momentum transport rate α , and (d) plasma β for model LT. The magnetic energy is averaged in the region $4 < \varpi/r_s < 10$, $|z/r_s| < 1$, and $0 \leq \varphi \leq 2\pi$.

Magnetic energy gradually decreases when $t > 55000t_0$. Figure 7c shows that $\alpha \sim 0.01$ in model LT. Since magnetic energy decreases, plasma β increases and stays around $\beta \sim 10$. Physical quantities shown in Figure 7 show short time scale oscillations and longer time scale ($\sim 4000t_0$) time variations. The latter is due to the time variation of the mass accretion rate from the outer region.

4. Formation of an Inner Torus and Its Oscillations

Figure 8 shows the snap shots of the density distribution. Figures 8a and 8b show the density distribution in $\varpi - z$ plane for model HT and LT, respectively. The density is averaged in the azimuthal direction. Figures 8c and 8d show the density distribution in $\varpi - \varphi$ plane averaged in $|z|/r_s < 1$. In model LT, an inner torus is created around $\varpi/r_s \sim 4 - 8$. The inner torus is deformed into a crescent-like shape. The inner torus is formed because angular

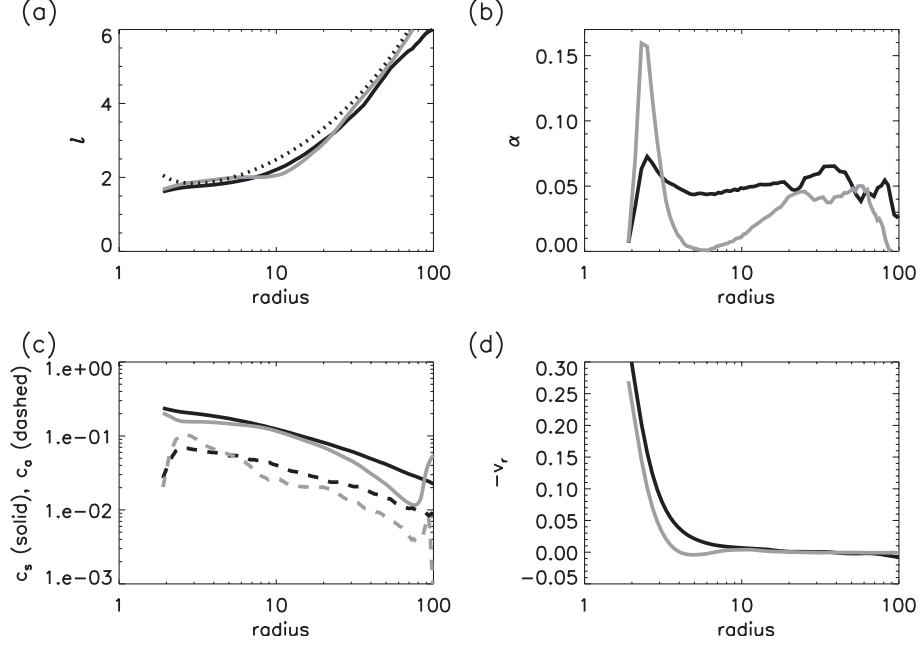


Fig. 9. Radial distribution of physical quantities averaged in $|z|/r_s < 1$ and in the azimuthal direction. Black curves show the distribution for model HT averaged in $23000 < t/t_0 < 29000$. Gray curves show the distribution for model LT averaged in $55000 < t/t_0 < 61000$. (a) Time-averaged specific angular momentum distribution. The dotted curve shows the Keplerian specific angular momentum using a Pseudo-Newtonian potential. (b) Radial distribution of the angular momentum transport rate defined by $\alpha \equiv \langle B_\varpi B_\varphi / 4\pi \rangle / \langle P \rangle$. (c) Solid curves and dashed curves show the sound speed and Alfvén speed, respectively. (d) Distribution of radial velocity.

momentum transport becomes inefficient. Figures 7a and 7b indicate that Maxwell stress decreases due to the decrease in magnetic energy. Magnetic energy decreases partly because magnetic flux is swallowed into the black hole with accreting gas and partly because magnetic energy dissipates by magnetic reconnection. The deformation of the inner torus into a crescent shape takes place due to the growth of the Papaloizou-Pringle instability (Papaloizou & Pringle 1984, Drury 1985).

When the disk is hot, since the inner torus is not formed, disk gas accretes to the black hole through dense, spiral channels (Figure 8c). This result is consistent with the result obtained by simulations of the hot disk reported by Machida & Matsumoto (2003).

Figure 9 shows the time-averaged radial distribution of physical quantities. The black curves show the results for model HT averaged in $23000 < t/t_0 < 29000$. The gray curve shows the result for model LT averaged in $55000 < t/t_0 < 61000$. Figure 9a displays the specific angular momentum distribution. The dotted curve shows the Keplerian specific angular momentum using pseudo-Newtonian potential. Since angular momentum continuously decreases in model HT, no inner torus is formed in this model. In model LT (dashed curve), since α is small, nearly constant angular momentum, inner torus is formed in $\varpi/r_s \sim 4 - 8$.

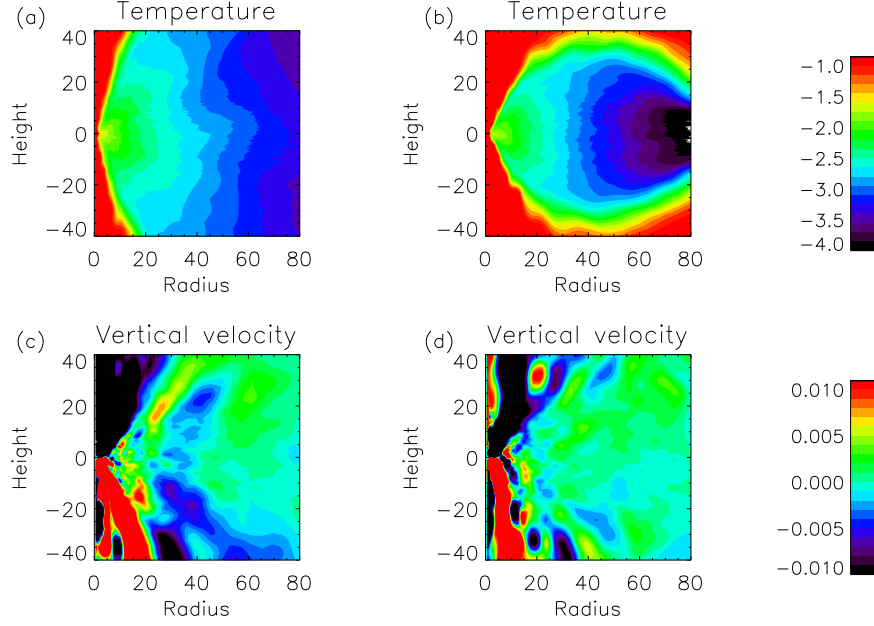


Fig. 10. (a) and (b) $\varpi - z$ slice of distribution of temperature $\log(T/T_0)$ averaged in the azimuthal direction. (c) and (d) distribution of the vertical velocity averaged in the azimuthal direction. (a) and (c) are at $t = 26950t_0$ for model HT, and (b) and (d) are at $t = 62750t_0$ for model LT.

Figure 9b shows the radial distribution of $\alpha \equiv \langle B_\varpi B_\varphi / 4\pi \rangle / \langle P \rangle$. Inside the inner torus, the angular momentum transport rate becomes very small. Solid and dashed curves in Figure 9c show the sound speed and Alfvén speed, respectively. Figure 9d shows the radial velocity. The accretion proceeds subsonically in $\varpi > 3r_s$. In model LT, accretion speed becomes very low in the inner torus.

Figure 10 shows the distribution of azimuthally averaged temperature (10a, 10b), and vertical velocity (10c, 10d). Figures 10a and 10b show that accreting matter is significantly heated up. Figures 10c and 10d show that mass outflow emerges from the disk with an average speed of $0.01c$. The outflow is anti-symmetric to the equatorial plane. The outflow is more powerful in model HT. By comparing Figures 8a and 10a, we can distinguish three regions; equatorial disk, hot funnel near the rotation axis, and outflows between the disk and the funnel. Accretion proceeds in the equatorial disk. A fraction of the accreting matter is ejected from the inner region of the disk.

Figure 11 shows the distribution of the azimuthal magnetic field (color) and magnetic fields depicted from the poloidal components of magnetic fields averaged in the azimuthal direction (curves). The azimuthal magnetic field is antisymmetric to the equatorial plane at this stage ($t = 26950t_0$ for model HT and $t = 62750t_0$ for model LT). Magnetic fields are turbulent inside the disk but show more coherent structures in the interface between the disk and the halo where mass outflow takes place. Magnetic field lines are stretched along this interface. A

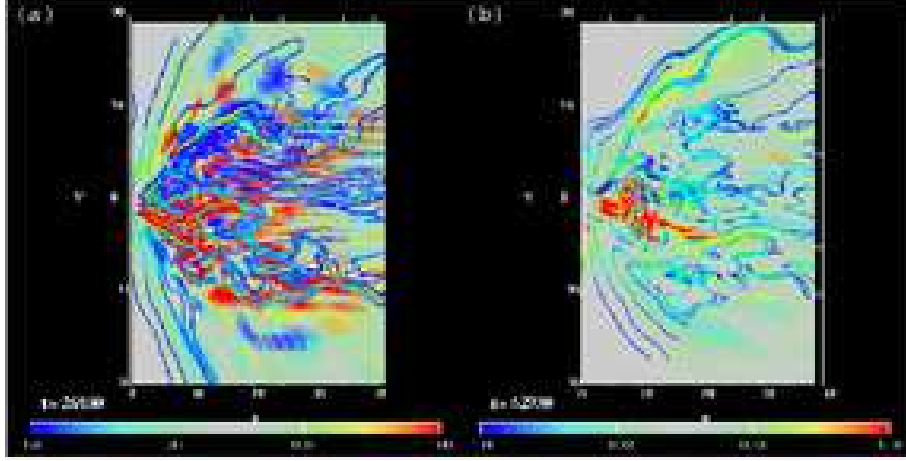


Fig. 11. Distribution of azimuthal magnetic field (color) and magnetic field lines (blue curves). The magnetic field lines are depicted from the poloidal components of magnetic fields averaged in the azimuthal direction. (a) model HT and (b) model LT .

large-scale poloidal magnetic field is created in the funnel near the rotation axis.

Figure 12 shows the snapshots of the density distribution on the $\varpi - \varphi$ plane for model LT. Density is averaged in the same region as that in Figures 8c and 8d. The inner torus deforms its shape from a circle into a crescent, and from a crescent into a circle, repeatedly.

The top panel of Figure 13 plots the time evolution of the ratio of the Joule heating rate to the magnetic energy averaged in $4 < \varpi/r_s < 10$, $|z|/r_s < 1$, and $0 \leq \varphi \leq 2\pi$. The ratio increases when magnetic energy is released (when $\langle B^2/8\pi \rangle$ decreases or ηJ^2 increases). The ratio changes quasi-periodically with a time scale of $\sim 1000t_0$.

The bottom panel of Figure 13 shows the time evolution of the amplitude of non-axisymmetric $m = 1$ mode (m is the mode number in the azimuthal direction) of the density. The amplitude of the azimuthal mode is computed by Fourier decomposing the density contrast

$$\rho/\langle \rho \rangle = \rho / \int_{2.9}^{5.3} \int_{-1}^1 \rho d\varpi dz . \quad (13)$$

The running average of the amplitude is plotted using the amplitude during $250t_0$ for each point. The gray curve depicts the same curve as that in Figure 13. The amplitude of $m = 1$ mode anti-correlates with $\eta J^2/\langle B^2/8\pi \rangle$. This indicates that the magnetic energy is released when the $m = 1$ mode disappears. The amplitude of the $m = 1$ mode also correlates with $\langle B_\varpi^2 \rangle$ (Figure 7b) and α (Figure 7c). They all show long timescale ($t \sim 4000t_0$) variation and short timescale ($t \sim 1000t_0$) oscillations. The peaks of the short timescale oscillations in the Fourier amplitude of the $m = 1$ mode in Figure 13 coincide with those in Figure 7.

Figure 14 shows the mass accretion rate measured at $\varpi = 4r_s$ (black), magnetic energy (gray), and the Fourier amplitude of the $m = 1$ mode for the density (dashed) for model LT. When the magnetic energy increases inside the inner torus, the mass accretion rate increases because the angular momentum transport rate increases as magnetic energy (and magnetic

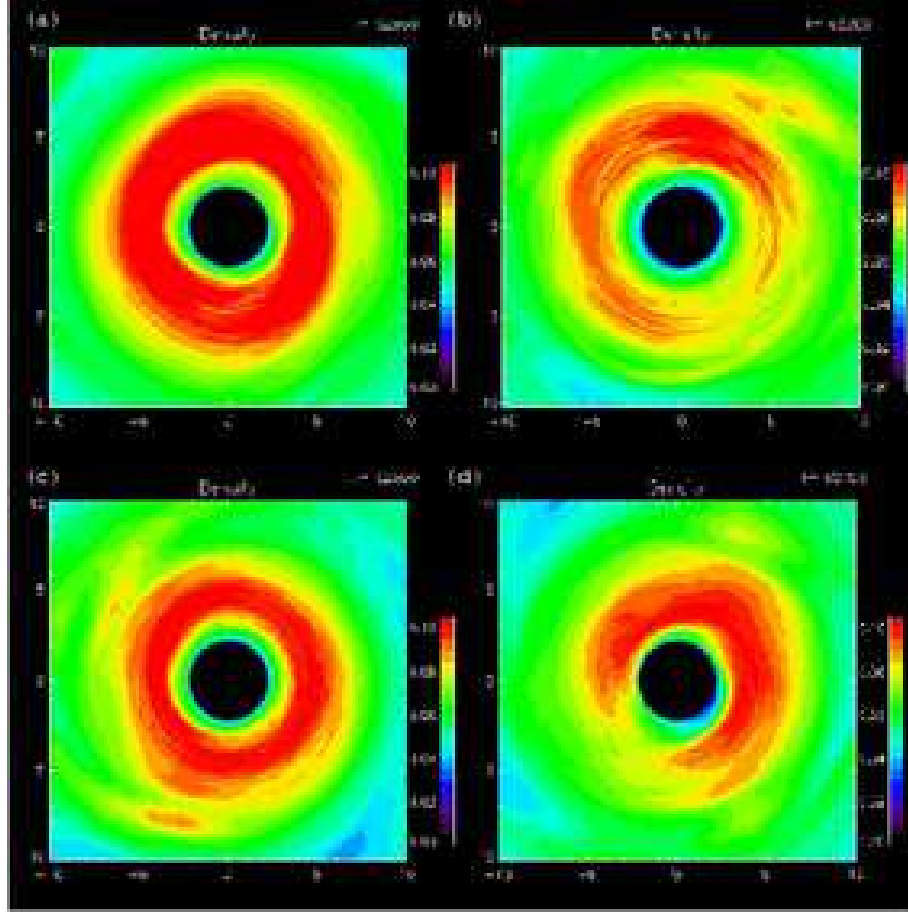


Fig. 12. Snapshots of the density distribution on $\varpi - \varphi$ plane for model LT.

stress) is accumulated in the torus. On the other hand, when the magnetic energy is released, the mass accretion rate decreases. The amplitude of the $m = 1$ mode (dashed curve in Figure 14) correlates with the magnetic energy (gray). The magnetic fields are amplified when the amplitude of the $m = 1$ mode increases. On the other hand, the amplitude of the $m = 1$ mode decreases when the magnetic energy is released. When the Maxwell stress decreases due to the decrease in magnetic energy, the Papaloizou & Pringle instability grows again inside the torus. Therefore, the torus deforms itself into a crescent shape. The interval between the magnetic energy releases in the inner torus is $\sim 1000t_0$.

Figure 15a shows the correlation between the amplitude of the $m = 1$ mode and the Joule heating rate normalized by the magnetic energy for model HT. The correlation function has positive peaks at $\delta t/t_0 = -2500, 0$ and 3000 . The positive correlation at $\delta t = 0$ indicates that magnetic energy is released when $m = 1$ spiral channel (see Figure 8c) develops. This result is consistent with that reported in Machida & Matsumoto (2003), where we showed that magnetic reconnection takes place in the spiral channel. Other peaks in the correlation function indicate that $m = 1$ mode develops quasi-periodically with interval $2500 - 3000t_0$.

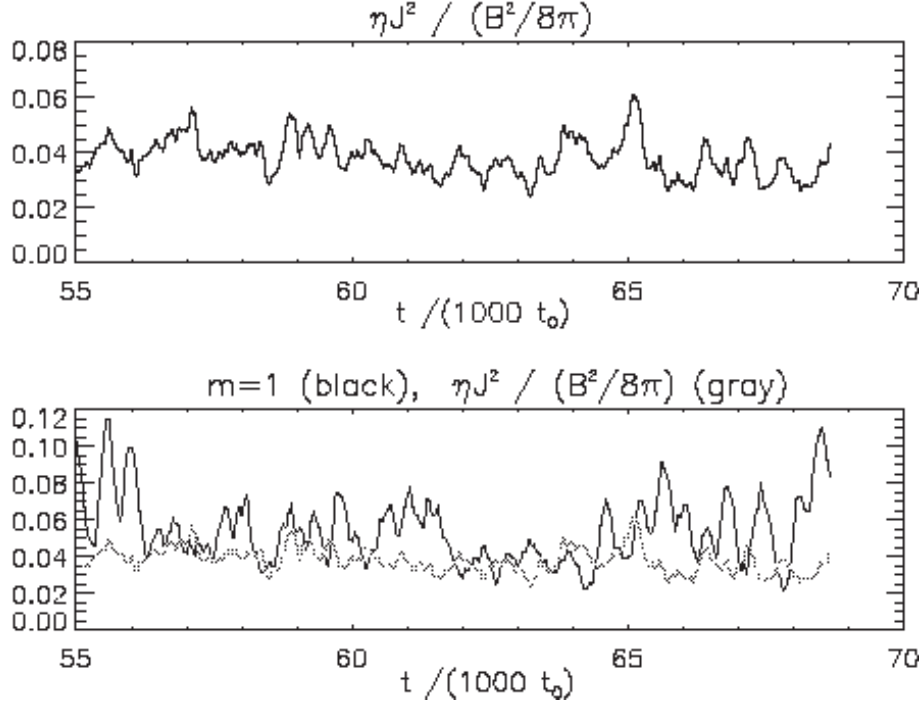


Fig. 13. (top) Time evolution of the ratio of the Joule heating rate to the magnetic energy for model LT. (bottom) Time evolution of the Fourier amplitude of the non-axisymmetric mode with the azimuthal mode number $m = 1$ computed from the density distribution (black). Gray curve depicts the same curve as that in the top panel.

Figure 15b shows the correlation between the amplitude of the $m = 1$ mode and the Joule heating rate for model LT. In contrast to that in model HT, no positive peak appears at $\delta t = 0$. Instead, negative peak appears at $\delta t/t_0 = -1200$ and positive peaks appear at $\delta t/t_0 = 1200, 2400$. It indicates that $m = 1$ mode anti-correlates with the Joule heating rate and that the growth of the $m = 1$ mode precedes the release of the magnetic energy by $\delta t \sim 1200t_0$.

Figure 16 shows the spatial distribution of the Fourier amplitude νP_ν of time variabilities in mass accretion rate for model HT in $23000 < t/t_0 < 32000$, and for model LT in $55000 < t/t_0 < 64000$. In model HT, various peaks appear at various radius. On the other hand, in model LT, low frequency QPOs around 10Hz appear in $5 < \varpi/r_s < 10$, where the inner torus is formed.

Figure 17 shows the Power Spectral Density (PSD) of the time variation of the mass accretion rate averaged in $3 < \varpi/r_s < 8$ and $|z|/r_s < 1$. Black and gray curves show PSD (νP_ν where P_ν is the Fourier power) for model LT and model HT, respectively. We adapted the data in the time range $23000 < t/t_0 < 32000$ in model HT and $55000 < t/t_0 < 64000$ in model LT.

The PSD for model LT has a broad low-frequency peak around 10Hz. This low-frequency peak corresponds to the oscillation involving amplification and release of magnetic energy in the inner torus. The PSD for model HT is flat in $\nu \leq 10\text{Hz}$, which means that $P_\nu \propto \nu^{-1}$ and

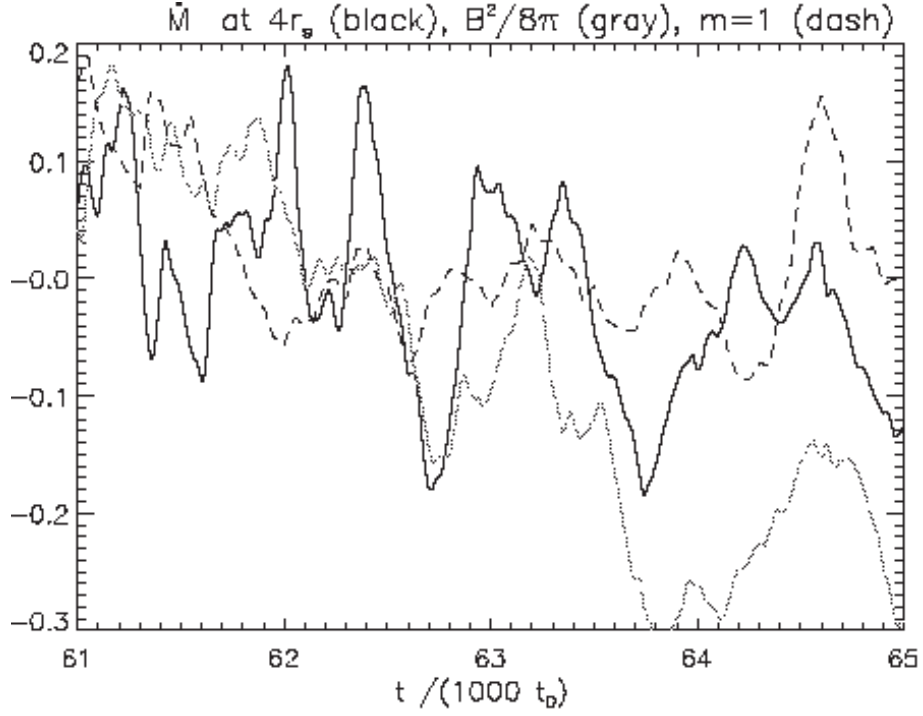


Fig. 14. Correlation of the time evolution of the mass accretion rate and magnetic energy in model LT. (black) Time evolution of the mass accretion rate measured at $\varpi = 4r_s$. (gray) Time evolution of the magnetic energy integrated in $4 < \varpi/r_s < 10$, $|z|/r_s < 1$, and $0 \leq \varphi \leq 2\pi$. (dashed) Fourier amplitude of the $m = 1$ mode in the density distribution. The curves are arbitrarily shifted in the vertical direction.

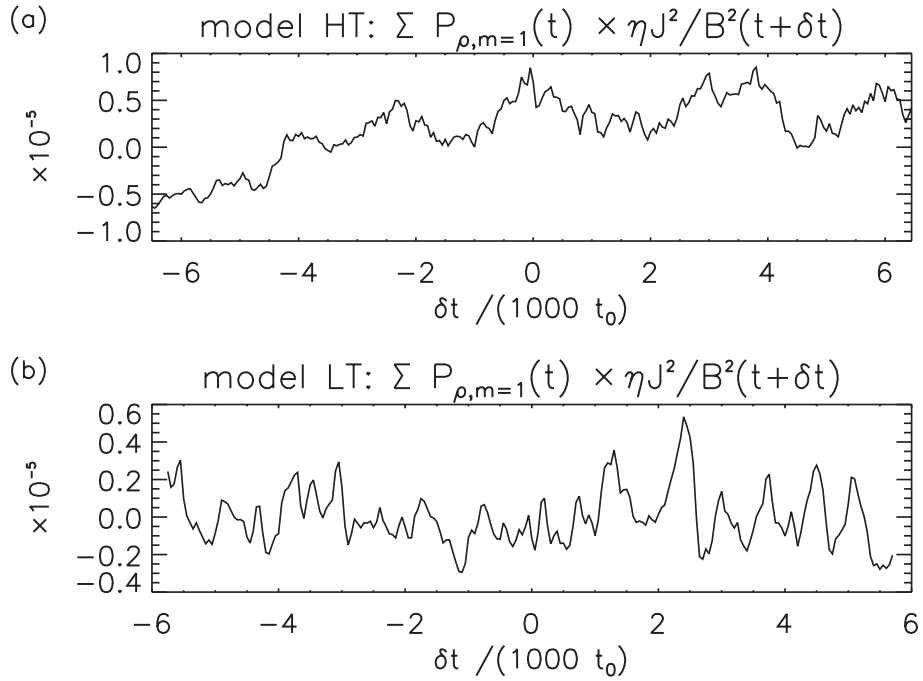


Fig. 15. Correlation function between the amplitude of the $m = 1$ mode and the Joule heating rate normalized by the magnetic energy. (a) is model HT and (b) shows model LT.

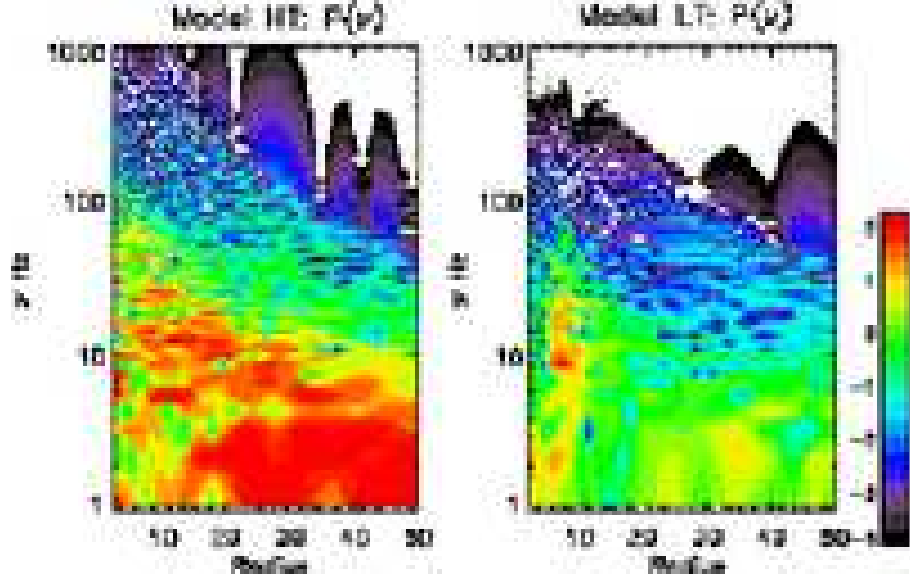


Fig. 16. Radial distribution of the PSD of the time variation of mass accretion rate for model HT measured in $23000 < t/t_0 < 32000$ (left) and for model LT measured in $55000 < t/t_0 < 64000$ (right).

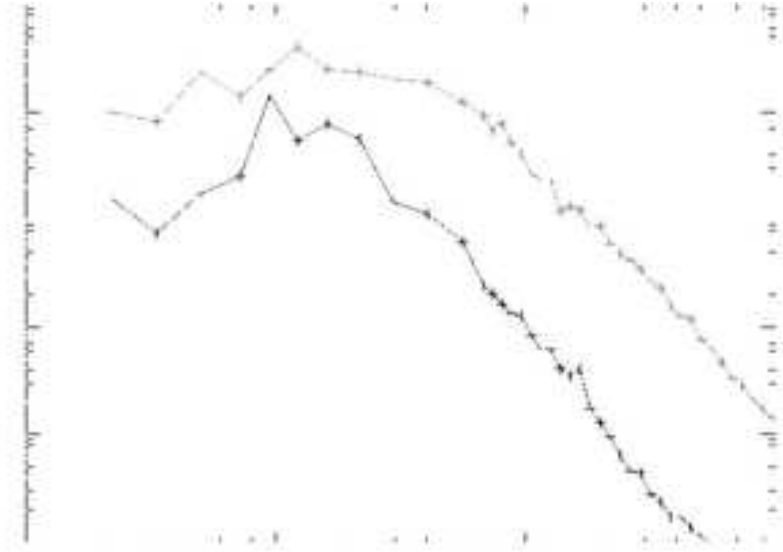


Fig. 17. Power spectrum νP_ν , where P_ν is the Fourier power of the time variation of mass accretion rate averaged in $2.5 < \varpi/r_s < 29$ and $|z|/r_s < 1$ for model LT (black) and for model HT (gray).

changes its slope around $\nu \sim 50\text{Hz}$. Since oscillations are excited at various radius in model HT, PSD shows flat spectrum. The PSD in model LT has a slope steeper than that in model HT in $30\text{Hz} < \nu < 100\text{Hz}$.

In model LT in Figure 17, a small peak appears at $\nu \sim 150\text{Hz}$. Based on the simulation using 32 azimuthal grid points, Matsumoto & Machida (2007) pointed out that a high-frequency QPO appears when the disk shows low-frequency ($\sim 8\text{Hz}$) sawtooth-like oscillations of magnetic energy. Here we confirmed that low-frequency QPOs and high-frequency QPOs coexist by a simulation including twice as many grid points in the azimuthal direction.

5. Discussion

In this paper, we studied the dependence of the structure and time variation of the black hole accretion flows on the gas temperature supplied from the outer region. When hot gas ($T \sim 10^{10}\text{K}$) is supplied, the angular momentum is transported efficiently all the way to the black hole. The average ratio of the Maxwell stress to gas pressure, $\alpha \equiv \langle B_\varpi B_\varphi / 4\pi \rangle / \langle P \rangle \sim 0.05$, consistent with previous simulations by Hawley (2001) and Machida & Matsumoto (2003). Such disks correspond to the radiatively inefficient, optically thin disk in the low/hard state of black hole candidates. Our simulation clearly showed the appearance of outflows with a maximum speed of $\sim 0.05c$ from such hot disks. The mass outflow rate \dot{M}_{out} is comparable to the mass accretion rate to the black hole. The magnetic fields are turbulent inside the disk but they show large-scale coherent structures near the rotation axis. Plasma flows out in the interface between the funnel and the accretion disk. The hot accretion flow shows time variations whose PSD is flat in $\nu \leq 10\text{Hz}$ when the mass of the central black hole is $M \sim 10M_\odot$.

When cool plasma is supplied, an inner torus is formed around $\varpi \sim 4 - 8r_s$. Such a torus is formed when the MRI-generated turbulent magnetic field is dissipated inside the disk. Since Maxwell stress decreases due to the decrease of magnetic energy, α decreases to $\alpha \leq 0.01$. Thus a nearly constant-angular-momentum torus is formed in the innermost region ($\varpi < 10r_s$) of the accretion flow. We found that the inner torus deforms itself into a crescent shape. Such deformation takes place due to the growth of the non-axisymmetric instability in geometrically thick tori (Papaloizou & Pringle 1984).

Such a non-axisymmetric structure enhances the growth of MRI. As magnetic energy increases, the angular momentum transport rate increases. Thus, the accretion rate increases. When the magnetic energy accumulated in the disk is released, the disk comes back to the weakly magnetized, axisymmetric torus. New cycle begins as magnetic energy is amplified by MRI. The period of the cycle is about $1000t_0$ in model LT. It creates a low-frequency peak around $4 - 8\text{Hz}$ in PSD of the mass accretion rate. Low-frequency QPOs sometimes observed in low/hard state and hard intermediate state (HIMS) of black hole candidates can be reproduced by such magnetic cycles. We also showed that a high-frequency QPO is excited when low-frequency QPO appears.

Let us discuss why the magnetic cycle is excited when low-temperature gas is supplied. When hot gas accretes, since the scale height of the gas is large, large eddies are formed in the magnetically turbulent disk and create a large scale coherent magnetic field which transports angular momentum efficiently. On the other hand, when low-temperature gas is supplied, since the scale height and eddy size become smaller, angular momentum is transported only in the local region. Thus the angular momentum is transported more efficiently in high temperature disks.

Low temperature plasmas can be supplied when cooling instability takes place in the outer disk. Machida et al. (2006) carried out a global 3D MHD simulation of black hole accretion flows by including radiative cooling. They showed that when the density of the outer disk is sufficiently high, cooling instability takes place. The outer disk shrinks vertically, and forms a magnetically supported, cool, optically thin disk. When such cool plasma accretes, the magnetic cycle may be excited in the inner region.

The amplitude of the $m = 1$ non-axisymmetric mode correlates positively with the Joule heating rate in model HT but anti-correlates in model LT. In model HT, since the angular momentum transport rate is large enough, mass smoothly accretes along the spiral channel, in which the magnetic fields are stretched and form a current sheet. Magnetic energy is released in such current sheets. Therefore, the amplitude of the $m = 1$ mode correlates with the Joule heating rate. On the other hand, in model LT, non-axisymmetric $m = 1$ pattern disappears when the magnetic energy is released.

Homan et al. (2005) pointed out that during the transition from the LHS to HSS, GX339–4 shows a sub-transition from HIMS dominated by power-law X-ray radiation to soft intermediated state (SIMS) dominated by radiation from an optically thick disk. They also showed that the low-frequency QPOs appear when the X-ray spectrum stays in HIMS and SIMS and sometimes in LHS. The high-frequency QPOs appear in the HIMS and SIMS. When the high-frequency QPO is observed, a low-frequency QPO is always observed in the X-ray spectrum. This tendency is consistent with our simulation results.

A number of theoretical models have been proposed for high-frequency QPOs. Abramowicz & Kuźniak (2001) proposed that high-frequency QPOs are formed by the resonance of radial and vertical oscillations. S. Kato (2001a) studied the excitation of high-frequency QPOs by resonance with the disk warp. In our simulation, a high-frequency peak appears around $\nu \sim 150Hz$ when the low-frequency oscillation is prominent. In our simulation, however, the low-frequency oscillation was weakened due to the heating of the inner torus. We expect that when the extra heating is extracted by radiative cooling, the magnetic cycle may continue and excite high-frequency QPOs. We would like to report the results of numerical simulations including radiative cooling in subsequent papers.

In this work, we treated the relativistic effect by using the pseudo-Newtonian potential. The accuracy of this approximation is worst near the black hole’s horizon especially for spinning

black holes. When we include the effects of black hole spin, the inner torus will be formed closer to the black hole. Thus, higher frequency QPOs will appear due to the oscillation of the inner torus. We should note that disk luminosity depends on the relativistic beaming and light bending. In subsequent papers, we would like to report PSDs obtained by relativistic ray-tracing of numerical results.

We are grateful to M.A. Abramowicz, S. Kato, W. Kuźniak, and M. Burusa for discussion. Numerical computations were carried out on VPP5000 at Center for Computational Astrophysics, CfCA of NAOJ (P.I. MM). This work is supported in part by Japan Society for the Promotion of Science (JSPS) Research Fellowships for Young Scientists (MM: 18-1907), and in part by Grants-in-Aid for Scientific Research of the Ministry of Education, Culture, Sports, Science, and Technology (RM: 17030003).

References

- Abramowicz, M. A. & Kuźniak, W. 2001, *A&A*, 374, L19
- Belloni, T. et al. 2006, *MNRAS*, 367, 1113
- Di Matteo, T., & Psaltis, D. 1999, *ApJ*, 526, L101.
- Drury, L. O’c 1985, *MNRAS*, 217, 821
- Gallo, E., Fender, R. P. & Pooley, G. G. 2003, *MNRAS*, 344, 60
- Hawley, J. F. 2001, *ApJ*, 554, 534
- Homan, J., Buxton, M., Markoff, S., Bailyn, C. D., Nespolo, E. & Belloni, T. 2005, *ApJ*, 624, 295
- Homan, J., & Belloni, T. 2005 in *From X-ray Binaries to Quasars: Black Hole Accretion on All Mass Scales*, edited by Maccarone, T. J., Fender, R. P., & Ho. L. C., Kluwer, in press
- Ichimaru, S. 1977, *ApJ*, 214, 840
- Kato, S. 2001a, *PASJ*, 53, 1
- Kato, S. 2001b, *PASJ*, 53, L37
- Kato, S. 2004, *PASJ*, 56, 905
- Kato, Y., Mineshige, S. & Shibata, K. 2004a, *ApJ*, 605, 307
- Kato, Y. 2004b, *PASJ*, 56, 931
- Kawaguchi, T., Mineshige, S., Machida, M., Matsumoto, R., & Shibata, K. 2000, *PASJ*, 52, L1
- Machida, M. & Matsumoto, R. 2003, *ApJ*, 585, 429
- Machida, M., Nakamura, K. E., & Matsumoto, R. 2006, *PASJ*, 58, 193
- Matsumoto, R., & Machida, M. 2007, *Proceedings of IAU Symposium 238*, Eds. V. Karas and G. Matt, Cambridge University Press, 37
- McClintock, J. & Remillard, R. 2006, in *Compact Stellar X-ray Sources*, eds, W. H. G. Lewin & M. van der Klis (Cambridge: Cambridge Univ. press)
- Narayan, R., & Yi, I. 1994, *ApJ*, 428, L13
- Narayan, R., & Yi, I. 1995, *ApJ*, 444, 231
- Negoro, H., Kitamoto, S., Takeuchi, M., and Mineshige, S. 1995, *ApJ*, 452, L49
- Oda, H., Nakamura, K. E., Machida, M., & Matsumoto, R. 2007, *PASJ*, 59, 457

- Okada, R., Fukue, J., & Matsumoto, R. 1989, PASJ, 41, 133
- Paczynski, B., & Witta, P. J. 1980, A&A, 88, 23
- Papaloizou, J. C. B., & Pringle, J. E. 1984, MNRAS, 208, 721
- Richtmyer, R. D., & Morton, K. W. 1967, Difference Methods for Initial-Value Problems, 2nd ed. (New York: Interscience Publishers) Chap. 13
- Rubin, E. L., & Burstein, S. Z. 1967, J.Comp.Phys., 2, 178
- Shakura, N. I., & Sunyaev, R. A. 1973, A&A, 24, 337
- Shaposhnikov, N., Swank, J. Shrader, C. R., Rupen, M., Beckmann, V., Markwardt, C. B., & Smith, D. A. 2006, ApJ, 655, 434
- Yokoyama, T., & Shibata, K. 1994, ApJ, 436, L197